DTIC COPY

REPORT DOCUMENTATION PAGE

Form Approved
OMB No. 0704-01-0188

PLEASE DO NOT RETURN YOUR FORM TO THE ABOVE ADDRESS.

1. REPORT DATE *(DD-MM-YYYY)*	2. REPORT TYPE	3. DATES COVERED *(From - To)*
10-07-2009	REPRINT	

4. TITLE AND SUBTITLE

The Impact of Geometry on Observations of CME Brightness and Propagation

5a. CONTRACT NUMBER

5b. GRANT NUMBER

5c. PROGRAM ELEMENT NUMBER
0630401F

6. AUTHORS
J. S. Morrill[1]
R. A. Howard[1]
A. Vourlidas[1]
D. F. Webb[2,3]
V. Kunkel[4]

5d. PROJECT NUMBER
5021

5e. TASK NUMBER
RD

5f. WORK UNIT NUMBER
A1

7. PERFORMING ORGANIZATION NAME(S) AND ADDRESS(ES)

Air Force Research Laboratory /RVBXS
29 Randolph Road
Hanscom AFB, MA 01731-3010

8. PERFORMING ORGANIZATION REPORT NUMBER

9. SPONSORING/MONITORING AGENCY NAME(S) AND ADDRESS(ES)

10. SPONSOR/MONITOR'S ACRONYM(S)
AFRL/RVBXS

11. SPONSOR/MONITOR'S REPORT NUMBER(S)
AFRL-RV-HA-TR-2010-1058

12. DISTRIBUTION/AVAILABILITY STATEMENT
Approved for Public Release; distribution unlimited.

13. SUPPLEMENTARY NOTES
Reprinted from Solar Physics (2009) 259:179-197, STEREO Science Results at Solar Minimum issue. DOI10.1007/s11207-009-9403-0
 See continuation for author affiliations.

14. ABSTRACT
Coronal Mass Ejections (CMEs) have a significant impact on space weather and geomagnetic storms and so have been the subject of numerous studies. Most CME observations have been made while these events are near the sun (*e.g.*, SOHO/LASCO). Recent data from the *Coriolis*/SMEI and STEREO/SECCHI-HI instruments have imaged CMEs farther into the heliosphere. Analyses of CME observations near the sun measure the properties of these events by assuming that the emission is in the plane of the sky and hence the speed and mass are lower limits to the true values. However, this assumption cannot be used to analyze optical observations of CMEs far from the Sun, such as observations from SMEI and SECCHI-HI, since the CME source is likely to be far from the limb. In this paper we consider the geometry of observations made by LASCO, SMEI, and SECCHI. We also present results that estimate both CME speed and trajectory by fitting the CME elongations observed by these instruments. Using a constant CME speed does not generally produce profiles that fit observations at both large and small elongation, simultaneously. We include the results of a simple empirical model that alters the CME speed to an estimated value of the solar wind speed to simulate the effect of drag on the propagating CME. This change in speed improves the fit between the model and observations over a broad range of elongations.

15. SUBJECT TERMS
Coronal mass ejection; Solar corona; LASCO; SMEI; SECCHI

16. SECURITY CLASSIFICATION OF:			17. LIMITATION OF ABSTRACT	18. NUMBER OF PAGES	19a. NAME OF RESPONSIBLE PERSON
a. REPORT	b. ABSTRACT	c. THIS PAGE			Janet C. Johnston
UNCL	UNCL	UNCL	UNL	19	19B. TELEPHONE NUMBER *(Include area code)*

13. SUPPLEMENTARY NOTES (Continued)

1. Space Science Division, Naval Research Laboratory, Washington, DC USA

2. Institute for Scientific Research, Boston College, Chestnut Hill, MA 02467 USA

3. The work of David Webb was supported by the Space Vehicles Directorate, Air Force Research Laboratory, Hanscom AFB, MA 01731 USA

4. George Mason University, Fairfax, VA

Solar Phys (2009) 259: 179–197
DOI 10.1007/s11207-009-9403-0

The Impact of Geometry on Observations of CME Brightness and Propagation

J.S. Morrill · R.A. Howard · A. Vourlidas · D.F. Webb · V. Kunkel

Received: 31 January 2009 / Accepted: 16 June 2009 / Published online: 10 July 2009

Abstract Coronal mass ejections (CMEs) have a significant impact on space weather and geomagnetic storms and so have been the subject of numerous studies. Most CME observations have been made while these events are near the Sun (*e.g.*, SOHO/LASCO). Recent data from the *Coriolis*/SMEI and STEREO/SECCHI-HI instruments have imaged CMEs farther into the heliosphere. Analyses of CME observations near the Sun measure the properties of these events by assuming that the emission is in the plane of the sky and hence the speed and mass are lower limits to the true values. However, this assumption cannot be used to analyze optical observations of CMEs far from the Sun, such as observations from SMEI and SECCHI-HI, since the CME source is likely to be far from the limb. In this paper we consider the geometry of observations made by LASCO, SMEI, and SECCHI. We also present results that estimate both CME speed and trajectory by fitting the CME elongations observed by these instruments. Using a constant CME speed does not generally produce profiles that fit observations at both large and small elongation, simultaneously. We include the results of a simple empirical model that alters the CME speed to an estimated value of the solar wind speed to simulate the effect of drag on the propagating CME. This change in speed improves the fit between the model and observations over a broad range of elongations.

STEREO Science Results at Solar Minimum
Guest Editors: Eric R. Christian, Michael L. Kaiser, Therese A. Kucera, O.C. St Cyr.

J.S. Morrill (✉) · R.A. Howard · A. Vourlidas
Space Sciences Division, Naval Research Laboratory, Washington, DC, USA
e-mail: jeff.morrill@nrl.navy.mil

D.F. Webb
Institute for Scientific Research, Boston College, Chestnut Hill, MA, USA

D.F. Webb
Air Force Research Laboratory, Space Vehicles Directorate, Hanscom AFB, MA, USA
e-mail: david.webb@hanscom.af.mil

V. Kunkel
George Mason University, Fairfax, VA, USA
e-mail: valbona.kunkel@nrl.navy.mil

Keywords Coronal mass ejection · Solar corona · LASCO · SMEI · SECCHI

1. Introduction

Imaging of coronal mass ejections (CMEs) during the past several decades has been largely confined to events observed near the Sun. Such observations have been made by several instruments including those on *Skylab* (McQueen, 1974), *Solwind* (Sheeley *et al.*, 1980), SMM (Hundhausen, Burkepile, and St. Cyr, 1994), and OSO-7 (Koomen *et al.*, 1974) and at Mauna Loa Solar Observatory (Fisher *et al.*, 1981) with the largest number of space-based observations being made by the LASCO coronagraphs on SOHO (Brueckner *et al.*, 1995). Starting in 2003, images of CMEs have been made farther from the Sun by SMEI on the *Coriolis* spacecraft (Eyles *et al.*, 2003; Jackson *et al.*, 2004; Webb *et al.*, 2006) and since early 2007 by SECCHI on the pair of STEREO spacecraft (Howard *et al.*, 2008). These observations have led to measurements of CMEs at much greater angular distances (elongations) from the Sun. This has required a reevaluation of the methods used to convert angular measurements to distance from the Sun.

Although CMEs originate from most regions of the Sun, their visibility is affected by where they occur on the disk (Webb and Howard, 1994). Regardless, measurements at small elongations (*e.g.*, SOHO/LASCO) usually are reported with the assumption that they are in the plane of the sky at the limb. This assumption can lead to large underestimates of the true height, speed, and mass, which, in turn, leads to incorrect analysis for observations at large distances and elongations from the Sun. To properly track CMEs from the Sun into the inner heliosphere, we must include a more detailed treatment of the geometry. In this paper we discuss the impact of geometry on CME observations by LASCO, SMEI, and SECCHI and how geometry affects measurements of CME brightness and speed.

Several studies have examined the SMEI and LASCO observations (Webb *et al.*, 2009; Howard *et al.*, 2007; Kahler and Webb, 2007; Howard and Simnett, 2008; Bisi *et al.*, 2008; Howard and Tappin, 2008) and this continued analysis will provide an important source of comparison for the analysis of events that presumably will be observed by SECCHI during the upcoming solar maximum. The observations from the SECCHI instruments show CMEs propagating continuously from the Sun to large heights, whereas the combined LASCO and SMEI observations made prior to the launch of SECCHI have a significant gap between 8° and 20° from the Sun. To bridge this gap we are developing a method for determining the speed and trajectory of CMEs observed by the LASCO and SMEI instruments. These methods will also be applied to SECCHI observations.

Since the range of CME speeds near the Sun is much greater than the range of shock and ICME speeds at 1 AU (Woo and Armstrong, 1985; Gopalswamy *et al.*, 2001; Manoharan *et al.*, 2004), we consider two different cases, constant and time-varying CME speed. An example of this range of speeds was also addressed by Manoharan (2006), who examined speeds from LASCO and IPS data. For the time-varying case we use a simple model to force CME speeds to an estimate of the solar wind speed to simulate the effect of coronal drag. Although this time-varying model is extremely simplistic, this case yields a better simultaneous fit to observations at both large and small elongation. The development and application of a more physics-based model has been considered by other groups and we will examine this issue in more detail in a future study.

Understanding the impact of geometry on CME observations has become more important with the advent of recent heliospheric imagers, SMEI and SECCHI-HI. Although the SMEI observations lack the resolution of the SECCHI-HI observations, SMEI can observe at higher latitudes than SECCHI-HI and so the combined data set of LASCO and SMEI observations, made prior to the launch of STEREO, represent a unique data set from the most

recent solar maximum. However, as can be seen with the SECCHI observations, the lack of a data gap that exists with the LASCO – SMEI combined data set is extremely important and simplifies the analysis of CME observations as they propagate to large distances from the Sun. In this paper we examine the details of the geometry that affect CME observations and apply the resulting methods to several observations made by LASCO, SMEI, and SECCHI.

2. The Geometry of CME Observations

The basic geometry of CME observations is shown in Figure 1. Here we assume that the CME propagates radially along a given trajectory. The view in this figure is perpendicular to the plane that contains the observer – Sun line and the trajectory of the propagating CME. In our analysis, we refer to the angle between the plane of the sky at the limb and the CME trajectory as the launch angle. CME speeds in the LASCO CME catalog are calculated from elongation angles (the angular distance from the CME leading edge to Sun center) converted to distances projected onto the plane of the sky at the limb. This results in speeds that are lower limits of the true radial speeds. As a result, CMEs propagating along different trajectories with the same time rate of change of elongation will have different radial speeds. This will be true even with more accurate models of the large angular extent of CMEs than shown in Figure 1 (*e.g.*, an expanding flux rope). At larger elongations, as the launch angle increases, the same projected speed implies an increase in the actual radial speed of the CME and the projected speed is no longer a reasonable proxy for the radial CME speed. The radial speed is necessary to compare observations at different elongations, so we must account for the launch angle in these comparisons. Similar considerations will also impact mass determinations from all these instruments.

Two other points should be noted from Figure 1. First, CMEs that propagate away from the observer (backside events) will not be visible at large distances from the Sun primarily because of their distance from the Thomson surface (Vourlidas and Howard, 2006). As a result, backside events can be seen by LASCO and SECCHI coronagraphs at small elongation but they generally will not be visible to the SMEI and SECCHI heliospheric imagers at large elongation. Second, as was already mentioned, a significant data gap exists for the LASCO – SMEI combined data set in the 8° to 20° elongation range. From the LASCO and SMEI observations discussed in the following, this is an important region where significant changes in CME speed appear to occur.

Although the combined LASCO – SMEI data set contains a significant data gap, this generally is not the case for the SECCHI observations. The four SECCHI imagers that view the corona above the solar limb have continuous fields of view. These four instruments

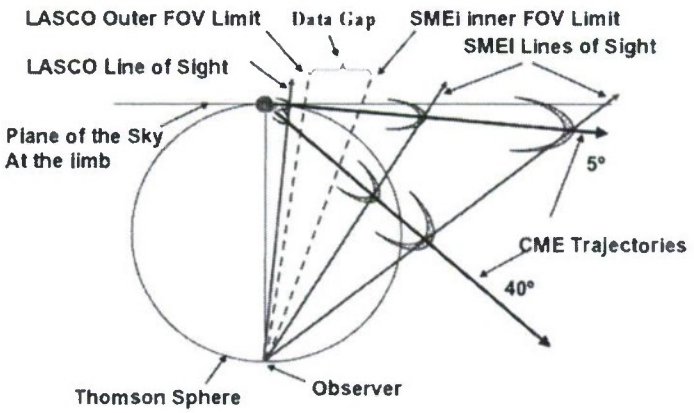

Figure 1 The basic geometry of LASCO and SMEI CME observations. For the SECCHI observations there is generally no data gap since the field-of-view (FOV) limits of COR-1, COR-2, HI-1, and HI-2 successively overlap to form a continuous FOV out to ~90°.

are the two coronagraphs with concentric fields of view, COR-1 and COR-2, and the two heliospheric imagers, HI-1 and HI-2. The nominal field-of-view limits are $0.4° - 1.1°$ for COR-1, $0.7° - 4.7°$ for COR-2, $4° - 24°$ for HI-1, and $18° - 88°$ for HI-2. These instruments are discussed in detail by Howard *et al.* (2008). As a result of this overlap, there is generally no data gap for the observations by these four instruments. In addition, UV disk observations are available from the SECCHI-EUVI imagers, which enable a clear connection from $1\,R_{\rm Sun}$ to $\sim$1 AU. As a result, CMEs can be seen over a broad range of elongations and this tends to simplify the analysis.

3. Brightness Variations of CMEs

Several factors govern the visibility of CMEs moving through the heliosphere, namely, their launch angle, their size, and their proximity to the Thomson surface or Thomson sphere. There are other issues such as how the CME is distorted as it propagates through the heliosphere but we do not address this here. The discussion that follows relies on the previous work on Thomson scattering by several authors (van de Hulst, 1950; Billings, 1966; Hayes, Vourlidas, and Howard, 2001) who provide detailed theoretical treatments of this process.

We begin by discussing the Thomson scattering efficiency of a single electron rather than a distribution of electrons. The Thomson surface is the locus of points that form right angles between lines from Sun center and the observer line of sight (Vourlidas and Howard, 2006). This surface is then where the Thomson scattering contribution is a maximum along the observer's line of sight. On either side of that point the scattering efficiency decreases symmetrically along this line of sight (Michels *et al.*, 1997). Since the Thomson surface is a sphere, the launch angle should be interpreted as the angle from the plane of the sky along any position angle, not just in the ecliptic plane. The position angle (PA) is measured counterclockwise from solar north (LASCO) or ecliptic north (SMEI or SECCHI) to the central axis of the propagating CME.

Brightness variations of CMEs have been discussed by Vourlidas and Howard (2006), who examine brightness changes beginning near the Sun. We focus on the region of elongation between 20° and 90°. Figure 2 gives the scattering intensity for a single electron as a function of the line-of-sight elongation for various launch angles. These curves include the effects of Thomson scattering, the distance from the Sun to the electron, and the scattering angle between the Sun and the observer. These single-electron results are then scaled up to the larger number of electrons in the CME.

The CME is an extended, diffuse object that presents an apparent surface brightness to the observer. One consequence of this is that distance between the observer and observed intensity from the CME cannot be determined. The intensity can change, however, with the distance from the Sun, owing to illumination differences, or with changes in the relative angles between the Sun, the CME, and the observer, all of which can impact the Thomson scattering coefficients.

Figure 2 shows that for large elongations, the intensity variation from events that originate on the backside of the Sun have a much steeper radial gradient, for all launch angles, than is the case for frontside events. Consequently, backside events will tend to be difficult to observe at large elongations. As noted by Vourlidas and Howard (2006), the ratio of the frontside to backside intensity for halo events at large elongations can be more than 100. Also, as shown in Figure 3, different parts of a backside CME may appear to be the leading edge because of enhancement along the line of sight. These issues may explain, in part, why LASCO sees many more events than SMEI (Webb *et al.*, 2006).

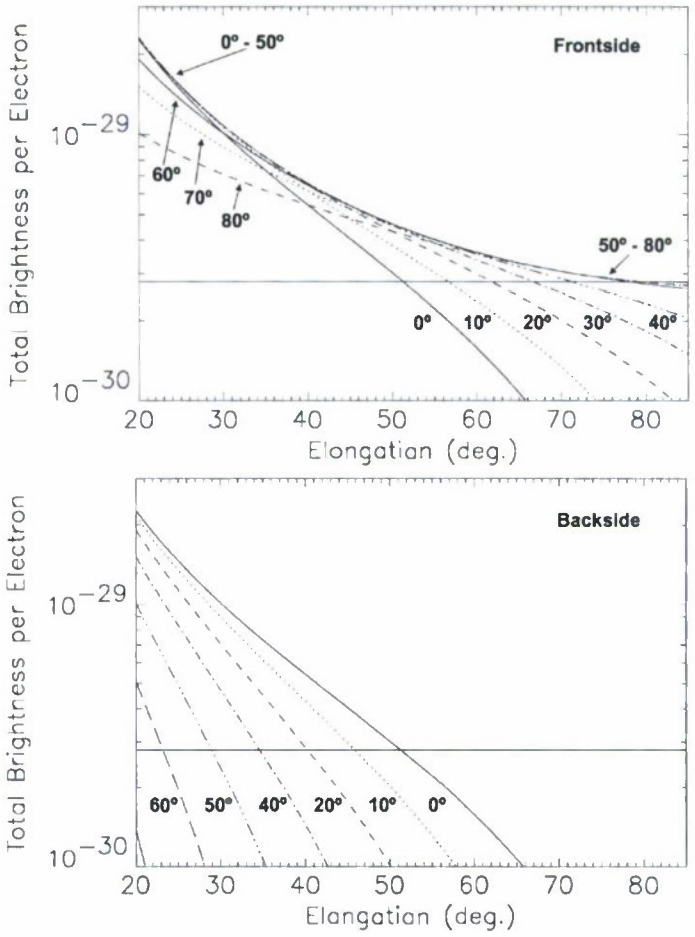

Figure 2 Total brightness per electron as a funetion of elongation for a range of launch angles for frontside events (top) and baekside events (bottom). These figures show why most baekside events will have low visibility at large distanees from the Sun but frontside events will be visible through mueh of the inner heliosphere.

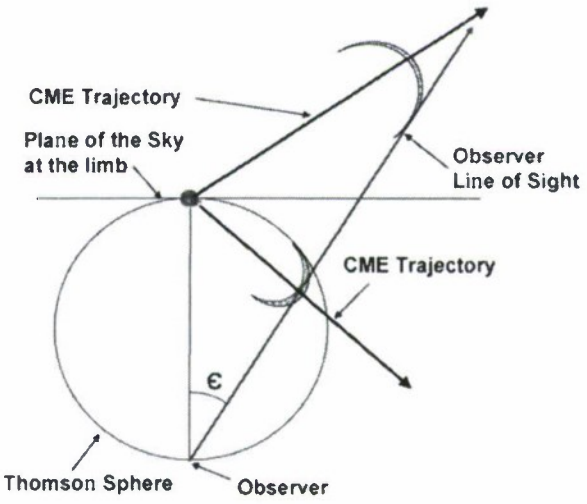

Figure 3 Geometric differenees between frontside and baekside CMEs observed along the same line of sight.

For frontside events the situation is more complex and depends strongly on launch angle. For example, events that originate at the limb (launch angle = 0°) quickly move off the Thomson sphere and thus the CME leading edge will become dimmer at large elongations. This issue was addressed elsewhere by using SMEI observations (see Figure 6 of Webb *et al.*, 2006). They indicate that limb CMEs appear at the inner edge of the SMEI field of view

then fade rapidly as would be expected from Thomson scattering. Roughly half of the SMEI events were reported to be in this category.

Frontside events that originate at launch angles farther from the limb will first start inside the Thomson sphere, cross it, and then propagate away from it. Unlike backside events, the Thomson scattering gradient for frontside events is much lower (see Figure 2). For launch angles $>20°$, the scattered intensity only decreases by about a factor of three for elongations from 30° to 80°. It is plausible that events could be visible at the Sun, become dim, and then brighten as they approach the Thomson sphere. This effect has been examined in 3D MHD simulations of the 28 October 2003 CME (Manchester *et al.*, 2008).

A real CME has an extended structure that affects observations in several ways. As it moves away from the Sun different parts could be identified as the leading edge by the observer. This effect can be seen in simulations and is discussed by Lugaz *et al.* (2009). From our previous analysis, the portion of the CME that is closest to the Thomson sphere will tend to be brightest. In addition, the parts of the CME that are tangent to the observer's line of sight will also tend to appear brighter because of the buildup of electrons along the line of sight. Further, in the case where the CME can be described as an expanding flux rope, the orientation of the flux rope can have a significant impact on the distribution of CME material with respect to the Thomson sphere, which will, in turn, affect the observed intensity. All these considerations, and others, complicate any interpretation of the propagation of CMEs. However, in the following discussion we assume that, as the CME propagates, the observed intensity is associated with the leading edge of the CME front that is expanding radially along the central axis.

4. CME Elongation versus Time

Observations of CMEs made by coronagraphs (*e.g.*, LASCO-C2/C3 or SECCHI-COR1/2) or heliospheric imagers (*e.g.*, SMEI or SECCHI-HI) measure the elongation angle associated with a bright feature propagating through the field of view. Several fitting techniques are used to convert from elongation to height above the solar surface, including the plane-of-the-sky assumption (Vourlidas and Howard, 2006), the point-P approximation (Howard *et al.*, 2006, 2007), fitting the observations with simulated flux-rope structures (Thernisien, Howard, and Vourlidas, 2006), the fixed-ϕ method (Kahler and Webb, 2007), and the analysis of Sheeley *et al.* (2008a, 2008b). The present method is the basis of our earlier analysis (Morrill, Howard, and Webb, 2006; Morrill *et al.* 2007; Morrill, Kunkel, and Howard, 2007) and follows the same assumptions as Kahler and Webb and Sheeley *et al.*

Here we present a technique to extract information about the launch angle and variable CME speed by fitting the CME elongations observed as a function of time. The position of a particle moving along a straight-line trajectory from the Sun (Figure 4) is described by the following equations:

$$\epsilon = \sin^{-1}\left[d\,\sin(\lambda)/r\right],$$
$$r = \left[R^2 + d^2 - 2R\,d\,\cos(\lambda)^{1/2}\right],$$

where ϵ is the observed elongation, $\lambda = 90° - \theta$, where θ is the launch angle, r is the observer–CME distance, and R is the observer–Sun center distance. We discuss two cases of CME speed: constant and time-varying. For constant speed, the Sun center–CME distance, d, is

$$d = vt + R_{\mathrm{Sun}}$$

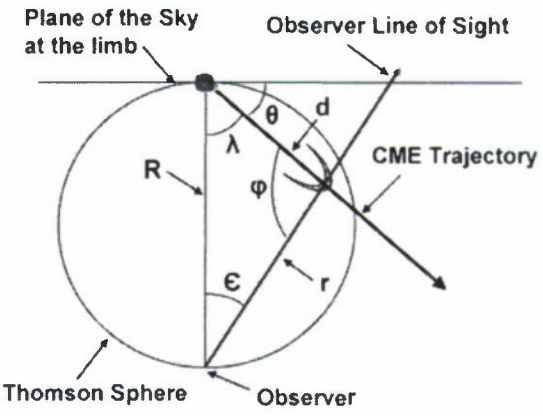

Figure 4 Parameters from the equations in Section 4 for a frontside CME.

and for the case of time-varying speed d is found from

$$d = \int_0^t v(t)\,\mathrm{d}t + R_{\mathrm{Sun}} \sim \sum_0^t v(t)\Delta t + R_{\mathrm{Sun}}.$$

Also, from the geometry of Figure 4 we get

$$d = R\sin(\epsilon)/\cos(\epsilon - \theta).$$

Here, t is the time from the surface and the various angles and variables are defined in Figure 4. An important point to note here is that for points on the Thomson sphere, $\epsilon = \theta$, so $d = R\sin(\epsilon)$ (Kahler and Webb, 2007).

This method generally ignores CME initiation but, as shown in figures discussed in the following, it fits LASCO and SECCHI-COR2 observations at heights between 2 and $20R_{\mathrm{Sun}}$ using constant speeds, so effects from CME initiation should not impact CME propagation at large elongations.

To better show the full range of observed elongation values at the same time, some of the following plots show the log of the elongation versus time. Figure 5 shows the predicted elongation of a CME leading edge propagating along several trajectories at 300 and 600 km s^{-1}. The various curves are for launch angle values between 0° and 75° from the limb (see caption). Events nearer the plane of the sky (0° – 30°) follow similar curves out to large elongations. Events originating nearer disk center (larger launch angle) follow curves that deviate significantly from the small launch angle curves.

5. Selecting Angles and Speeds

Because of the data gap between the two instruments, LASCO and SMEI observations are treated somewhat differently than the SECCHI observations. For the LASCO and SMEI observations we use an analysis procedure that initially treats observations from both instruments separately as follows. Using families of curves like those in Figure 5, the best fit to the observed elongations of a CME is determined from the best fit at constant speed for a set of launch angles ($\Delta\theta = 5°$). The best fit is found by minimizing the difference between predicted and observed elongations. Best fits for a set of LASCO and SMEI observations are shown in Figures 6(a) and (b), respectively. Here, various launch angle – speed combinations fit each data set within its range of elongations. Next, we select which angle – speed

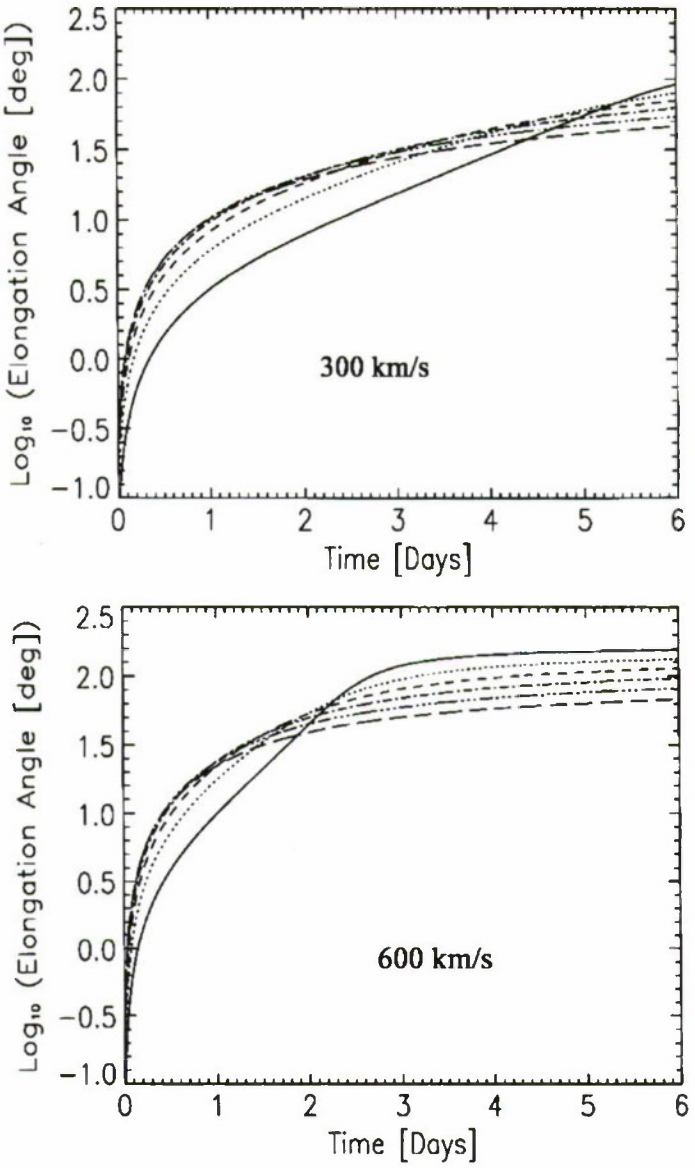

Figure 5 The log of the elongation versus time for a CME propagating at various launch angles from the plane of the sky. At time equal to 1 day, starting with the lowest curve and moving up, the associated launch angles are 75°, 60°, 45°, 30°, 15°, and 0° at 300 km s^{-1} (top) and 600 km s^{-1} (bottom).

combination is the best choice for the specific data set. This is done by examining either the CME speed projected on the plane of the sky (LASCO) or the range of observed elongations (SMEI). Ultimately, information from disk observations will be included in our analysis but we begin by first trying to extract this information from the CME observations directly.

For the LASCO data, the optimum launch angle – speed combination is determined by the best fits to the plane-of-the-sky CME speed. Here the predicted speed at each launch angle is scaled by the cosine of this angle and compared to the reported CME speed. For the SMEI data, the optimum launch angle – speed combination is taken as the one with the launch angle closest to the midpoint of the observed elongation values. This approximation is based on the aforementioned visibility arguments and assumes that the CME is best observed when in the region of the Thomson sphere where $\epsilon = \theta$. This is similar to the basic assumption of the point-P approximation. Since SMEI observations begin near 20° elongation and we do not account for the extended size of CMEs, this method can overestimate the optimum launch angle of the SMEI observations.

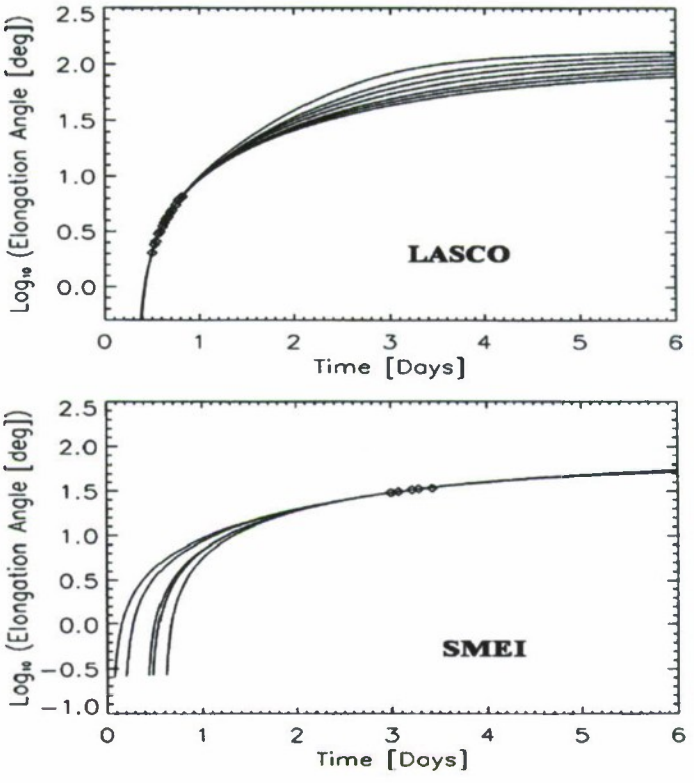

Figure 6 Fits of elongation to observations by LASCO (top) and SMEI (bottom) (see text for details).

Although this method can yield good fits to either the LASCO or SMEI observations (see Figure 6), the constant speed estimates generally do not yield fits to both data sets at the same time. To model the effect of time-varying CME speed we introduce a term that changes the CME speed as it propagates beyond $20R_{\text{Sun}}$. The following results are from analysis for both constant and time-varying speed.

For the SECCHI observations the method is much simpler if we examine an event where there is no data gap and the observations cover a range of elongations beyond 30°. Here we assign a launch angle from SECCHI-EUVI disk images and fit the CME observations between 10 and $20R_{\text{Sun}}$ to a constant speed. In the SECCHI example presented in the following, two speeds were used to fit the observations below $20R_{\text{Sun}}$. Above $20R_{\text{Sun}}$ we compare the constant and variable speed profiles to the observations and select the speeds that result in the best overall fit. For the variable speed profiles we use the same simple model (see next section) to alter the CME speed to simulate the effect of drag.

6. Results and Discussion

6.1. LASCO and SMEI Observations

Using these methods we have fit several CMEs with constant speed profiles observed in the northwest quadrant during the period 15 – 24 February 2003. Images of one of the three main events that occurred during this time period are shown in Figure 7, which shows images from EIT, LASCO-C3, and SMEI. These fits appear in Figure 8. Fits to LASCO data with solid lines are out of the plane of the sky (launch angle $\geq 15°$) whereas dotted lines are near the plane of the sky (launch angle $< 15°$). Fits to SMEI data are the dashed lines. The lack of a clear connection between SMEI and LASCO fits implies changes in the CME speed

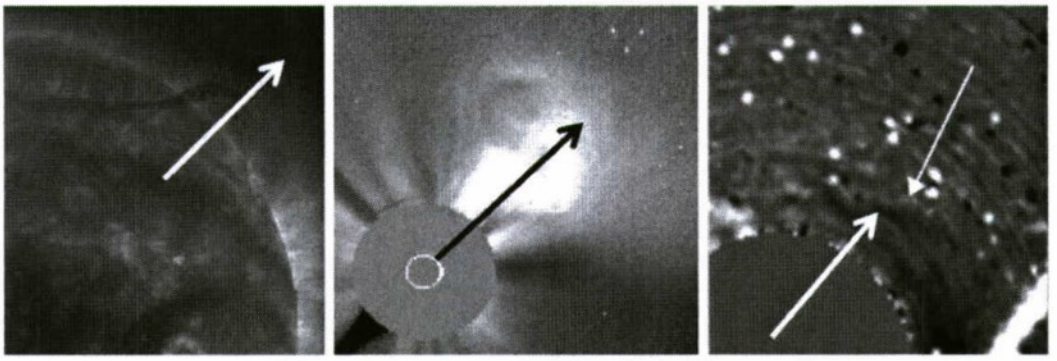

Figure 7 Images of one of the three main events that occurs during this time period. From left to right these are images from EIT (195 Å), LASCO C3, and SMEI. The EIT image shows the orientation of the large prominence associated with this event. The three arrows pointing upward to the right indicate the approximate direction of propagation of this event. The second arrow in the SMEI image points to the leading edge of the observed CME (Howard *et al.*, 2007).

as it propagates into the heliosphere. These plots show the difficulty of associating CMEs observed in LASCO with ones observed in SMEI and how sensitive this association is to the CME speed profile. This result, in addition to the CME speed differences at the Sun and at Earth, demonstrates that simple associations based on the assumption of constant speed overly simplify the problem of determining the speed and trajectory of CMEs as they propagate into the heliosphere.

Numerous authors have included a drag force when modeling CME propagation (Chen, 1996; Cargill, 2004; Tappin, 2006; Howard *et al.*, 2007). In the present analysis we use a simple model to simulate the effect of coronal drag and to change the CME speed as it moves through the heliosphere. By fitting these events we derive an estimate of the CME speed as a function of height. We apply this term to the constant CME speed profile estimated from the LASCO observations and this yields a better fit to the SMEI observations. The speed is changed by a term with the functional form $[\pm 0.5(d/2)^{3/4}\Delta V^2]$, where ΔV is the difference between the CME and solar wind speeds and d is the Sun center – CME distance in AU. This is a completely empirical rather than a physical model and was used because it improved the connection between LASCO and SMEI observations.

In this fitting process, this term is included at heights $\geq 20 R_{\rm Sun}$. This height was chosen because of the relatively constant speeds observed throughout the LASCO C3 field of view. The terminal (solar wind) speed is set to 400 km s^{-1} for the first six events and to 470 km s^{-1} for the last two events. These terminal speeds were chosen based on the difference in latitude of these events, how well the selected speed improved the fit, and rough estimates of the solar wind speeds indicated by results of the Wang – Sheeley model (Wang and Sheeley, 1994). The sign of this term depends on whether the initial CME speed is greater or less than the terminal (solar wind) speed. As expected, the CME speed is driven toward the solar wind speed. When these time-varying speeds are included in the fit shown in Figure 8 (bottom), the connection between the LASCO and SMEI events is significantly improved.

To further show the relation between the LASCO and SMEI events and the effect of varying the CME speed, these results and observations are plotted on a linear scale in Figure 9. This figure shows the measured elongation (a, b) and calculated heights (c, d) from both LASCO and SMEI (data points) and the fits to the LASCO observations. These fits are extended to large elongations and higher heights as solid and dashed lines, where the

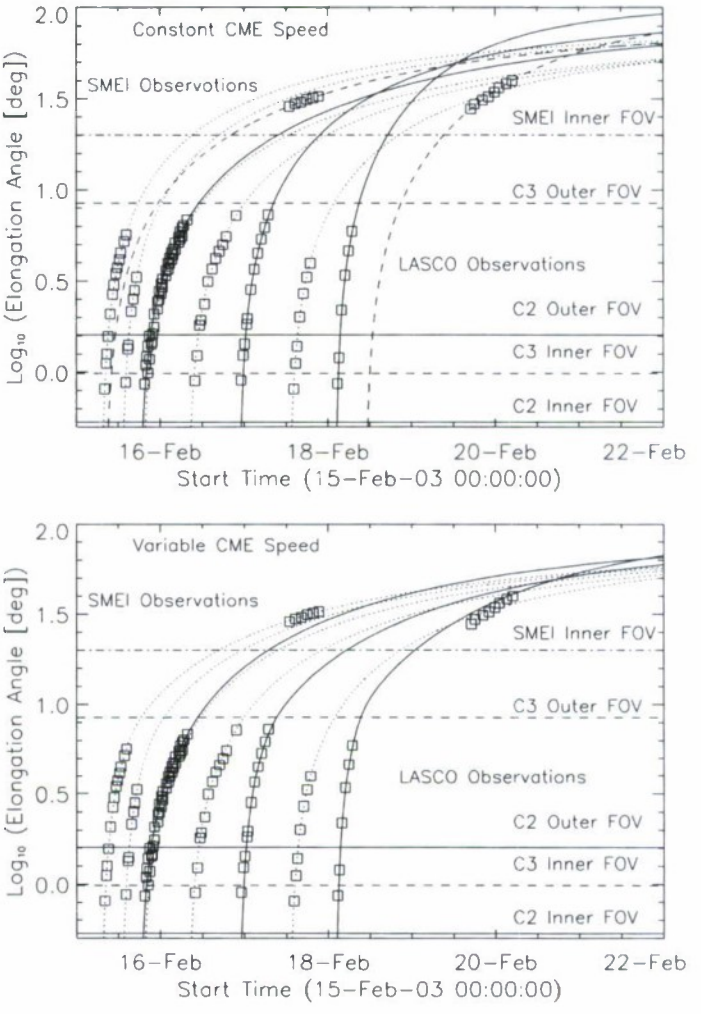

Figure 8 (Top) Fits to LASCO and SMEI CME observations at constant speed. The fits to LASCO data are the solid lines (launch angle $\geq 15°$) and dotted lines (launch angle $< 15°$). The fits to the SMEI data are the dashed lines (17 February, PA = 280°, launch angle = 30°, $V = 400\ \mathrm{km\,s^{-1}}$; 19 February, PA = 330°, launch angle = 35°, $V = 640\ \mathrm{km\,s^{-1}}$). (Bottom) The same as the top figure except time-varying-speeds were used to fit the LASCO data and the fits to the SMEI data have been dropped.

meaning of the solid and dashed lines is the same as in Figure 8. The three main (brightest) CMEs are indicated by larger symbols and thicker lines. These are the first, sixth, and eighth events. (Note that events 3 and 4 overlap each other.) Figures 9(a) and (c) show fits with constant speed derived from the LASCO observations. The fits in these two figures show no clear connection between the LASCO and SMEI observations as shown in Figure 8 (top). However, Figures 9(b) and (d) show that, by allowing the CME speed to vary, the fit for both elongation and height is improved and shows a much clearer connection between LASCO and SMEI observations. The lack of a SMEI event on 18 February (Figures 8 and 9) was probably due to a degradation in SMEI data during that time period because of the spacecraft's passage through a region of enhanced particles.

The CME speed profiles used in Figures 9(b) and (d) are shown in Figure 10 and indicate a rapid change in the CME speed between 20 and $60R_{\mathrm{Sun}}$ for the elongation and height profiles to match both LASCO and SMEI observations.

6.2. SECCHI Observations

For the case of a CME observed by SECCHI we have examined an event that occurred on 15 May 2007. Figure 11 shows several images of this event from the STEREO-A SECCHI imagers, EUVI, COR-2, and HI-1. This CME was observed in all five SECCHI-A imagers.

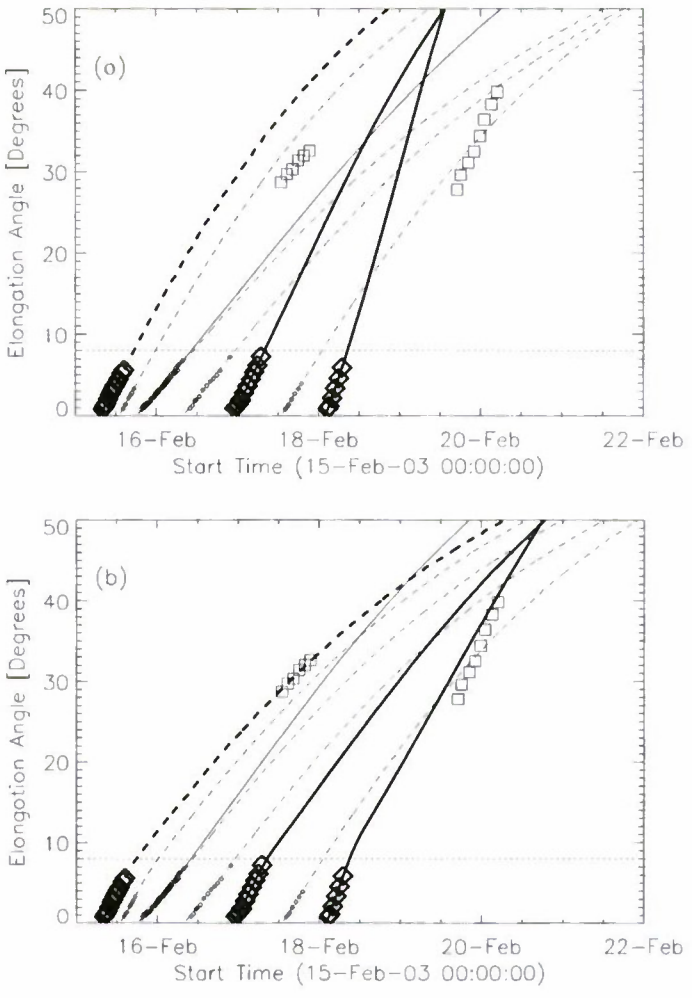

Figure 9 Elongation–time (a and b) and calculated height–time (c and d) plots on a linear scale for the eight events shown in Figure 8 overplotted with the SMEI observations. In all four figures the three main events are indicated by the larger symbol size and thicker lines. As with Figure 8, the dashed lines are best fit with launch angles less than 15° and the solid lines are for 15° or greater. Constant CME speed was used in Figures 9(a) and (c), and variable CME speed was used in Figures 9(b) and (d). The horizontal dotted line is the approximate limit of the C3 field of view.

It was also observed by LASCO but we have included only the SECCHI observations in this analysis. This event began about 18:00 UT and was observed until early on 18 May. In this analysis we followed the observed leading edge along the PA shown in Figure 11. The angle from the plane of the sky was estimated to be ~38° from an active region observed in EUVI (see Figure 11). This is the launch angle we used in our fitting of these observations.

As with the LASCO-SMEI fits, Figure 12 compares the SECCHI observations to fits with constant (Figure 12, top) or variable (Figure 12, bottom) CME speeds. Figure 12 (top) shows fits with several constant speeds. Figure 12 (bottom) shows fits that start with these same constant speeds but then the speed was altered to simulate the impact of drag using the same functional form that was used in our LASCO–SMEI analysis. The initial constant speeds used in these figures are 325, 435, 550, and 650 km s^{-1}. The two lowest speeds, 325 and 435 km s^{-1}, were chosen because they fit COR-1 and COR-2 observations, respectively. The larger speeds, 550 and 650 km s^{-1}, were chosen to show profiles produced by higher speeds. The 435 km s^{-1} curve fits the HI-1 observations fairly well but this curve rises above the observations in the HI-2 field of view, indicating the need for a slight correction at large elongation. The CME speed is altered by using the same term discussed earlier except the terminal speed used here is 415 km s^{-1} and was chosen since it produced the best fit to the HI-2 observations.

Figure 9 (*Continued*)

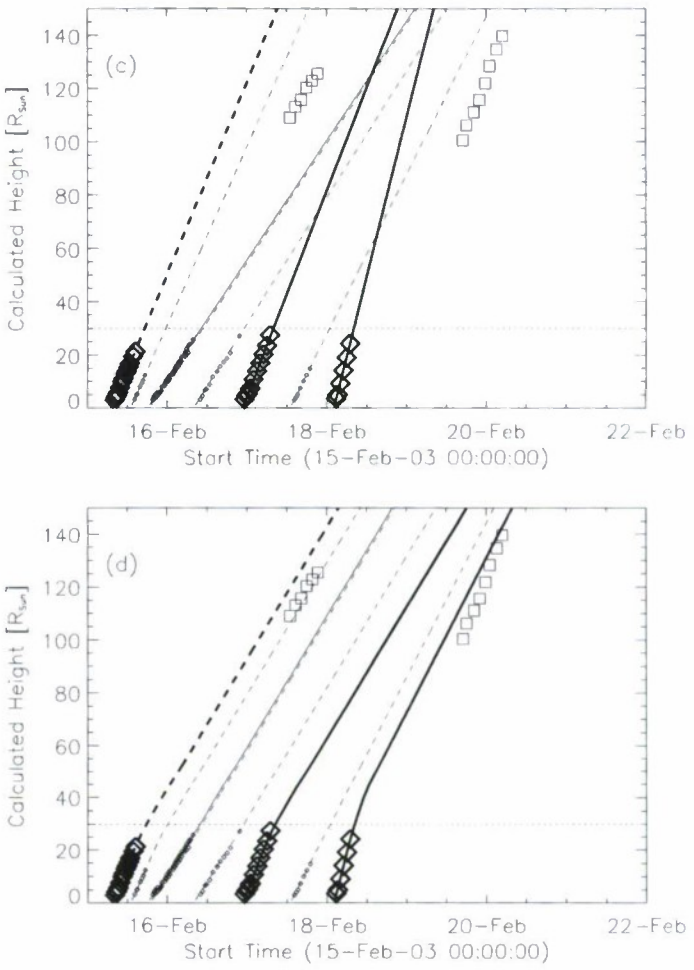

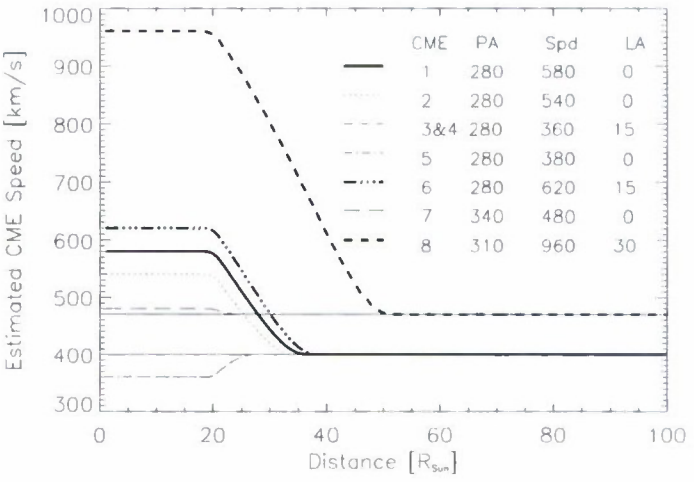

Figure 10 CME speed profiles modified by the drag term. The CME numbers are for LASCO events in Figure 4 numbered left to right. The units for the tabulated values are [°] for position angle (PA), [km s^{-1}] for speed (Spd), and [°] for launch angle (LA).

In Figure 13 the results from Figure 12 are shown on a linear scale. Two different values of maximum elongations were used for these figures to compare the fits to different sets of observations at larger elongations. Figures 13(a) and (b) show the observations and fits up to elongations of 12° and Figures 13(c) and (d) show these comparisons out to 40°. As

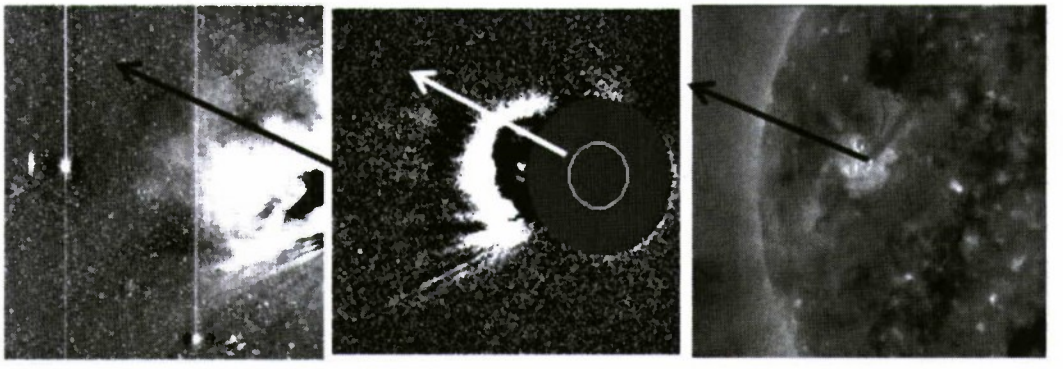

Figure 11 Images showing the main event that occurs during this time period. From right to left these are images from STEREO-A EUVI, STEREO-A COR2, and STEREO-A HI-1. The EUVI image shows the location of the active region that produced this event. The three arrows pointing upward to the left indicate the approximate direction of propagation of this event.

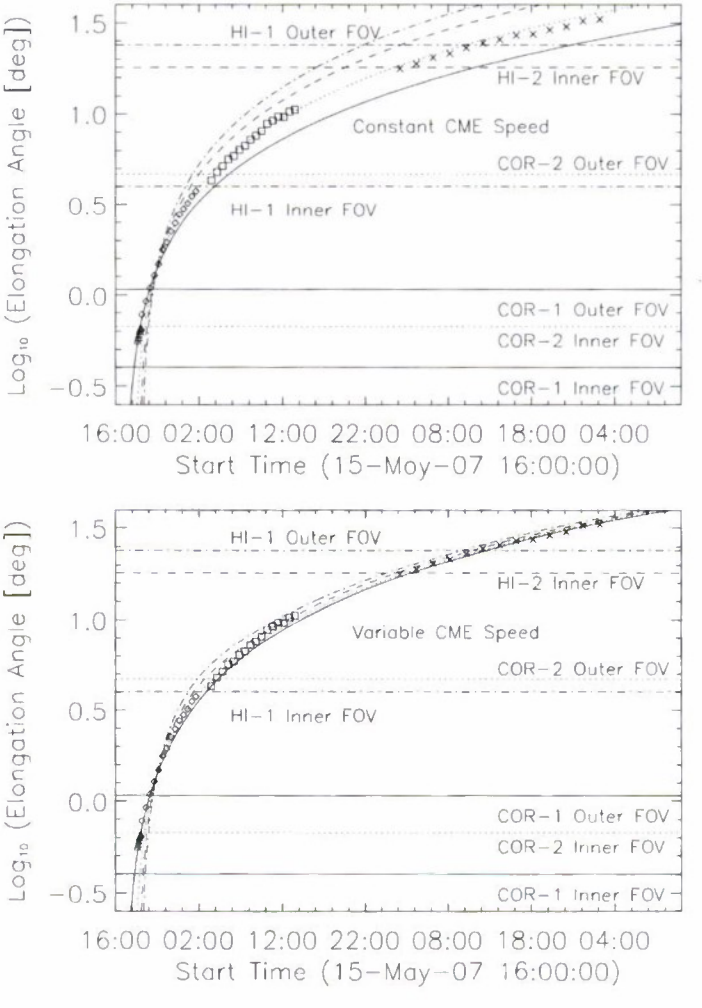

Figure 12 Fits to STEREO observations at constant speed (top) and variable speed (bottom). The four lines are calculated elongations at constant initial speeds of 325 km s^{-1} (solid line), 435 km s^{-1} (dotted line), 550 km s^{-1} (dashed line), and 650 km s^{-1} (dot-dash line). The same function and coefficient were used in the bottom figure as were used in Figures 8 and 9. The final speed used in this case was 415 km s^{-1}.

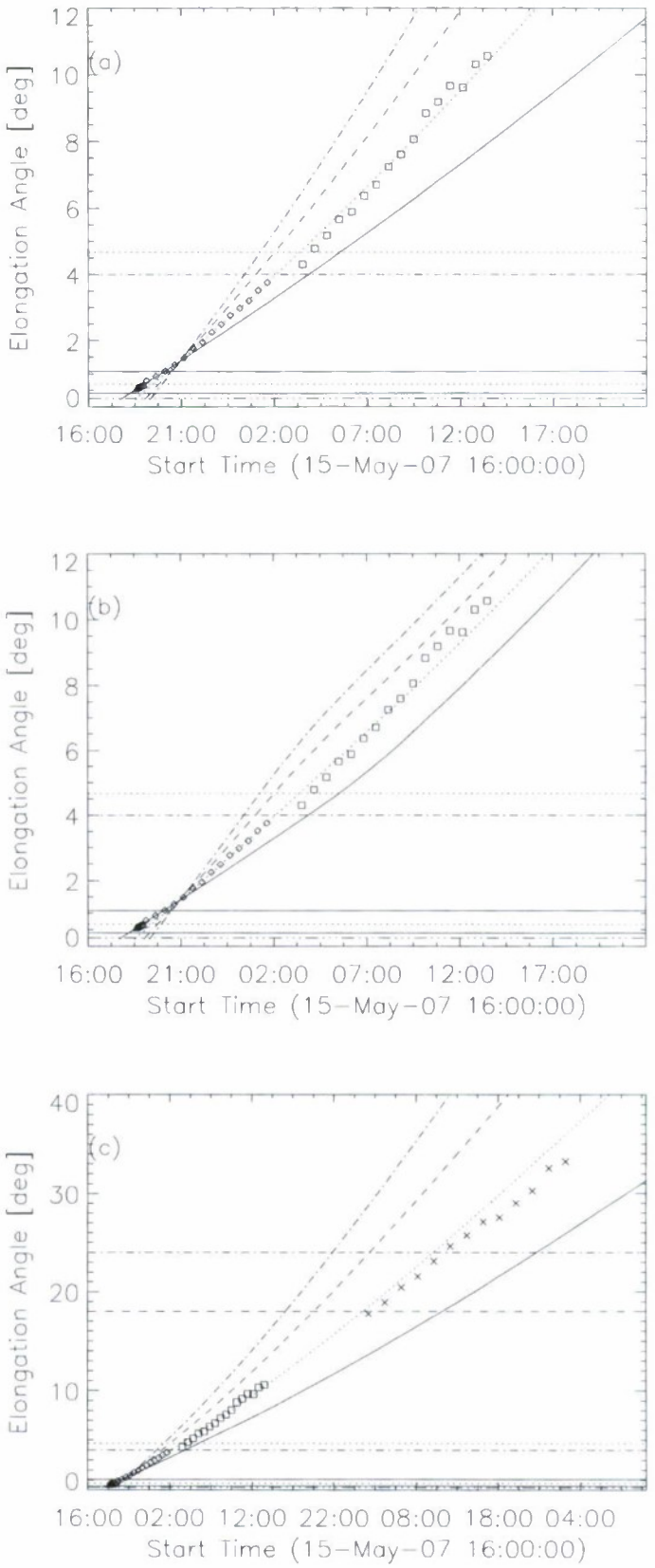

Figure 13 Elongation – time plots on a linear scale for two different sets of limits. Constant CME speed was used in Figures 13(a) and (c), and variable CME speed was used in Figures 13(b) and (d). From the top down the horizontal lines or the field-of-view limits are (a and b) COR-2 outer field of view (dotted), HI-1 inner (dash-dot), COR-1 outer (solid); (c and d) HI-1 outer (dash-dot), HI-2 inner (dashed), COR-2 Outer (dotted). The initial speeds are 325 km s^{-1} (solid line), 435 km s^{-1} (dotted line), 550 km s^{-1} (dashed line), and 650 km s^{-1} (dot-dash line).

Figure 13 (*Continued*)

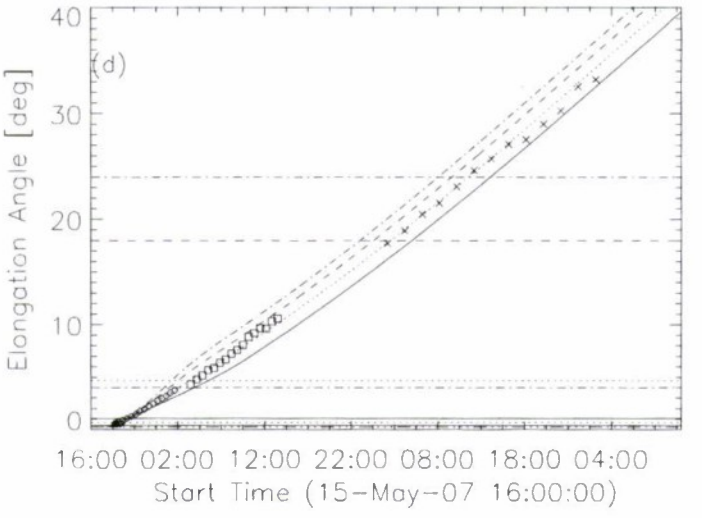

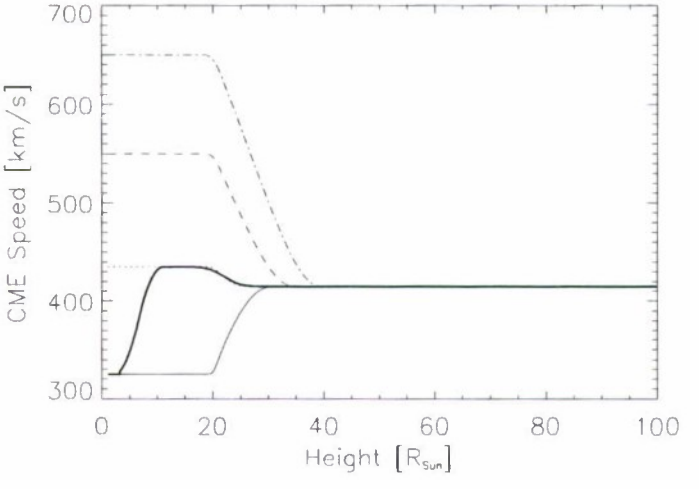

Figure 14 CME speed profiles modified by the same function as was used in the LASCO SMEI results. As before the speed is held constant until $20R_{\mathrm{Sun}}$. The heavy solid line is an estimate of the speed profile based on the fits at the various elongations. The terminal speed is 415 km s^{-1}. The line types correspond to the curves in Figure 12(b) and Figures 13(a) and (b).

previously noted, the best fit to the HI-1 observations shown in Figures 13(a) and (b) is the 435 km s^{-1} curve. Figure 13b also shows the effect of driving these profiles to a specific terminal (solar wind) speed from several different initial speeds. In all cases the fitted CME speed profiles reach the terminal speed relatively quickly but they are offset in time because of their different initial speeds. Figures 13(c) and (d) show these curves in the region of the HI-2 observations. The linear plot (Figure 13(c)) shows more clearly than the log plot (Figure 12, top) that the constant speed profile that best fits the lower height observations (435 km s^{-1}) rises above the observation in the HI-2 field of view. Although the correction is very slight in this case the improved fit (dotted curve) is shown in Figure 13(d). This figure also shows the time offset of the other fits with different initial speeds.

The best-fit speed profile from the analysis of this event is shown in Figure 14 as the heavy solid line. The other curves are the speed profiles used to calculate the elongation curves in Figures 12 (bottom) and Figures 13(b) and (c), with the line type associated with different speeds being the same in all three figures. The rate of transition between the 325 and 435 km s^{-1} speeds is an estimate since a detailed analysis of these profiles was not performed. It is clear that a significant transition to a stable speed was achieved below $20R_{\mathrm{Sun}}$

in Figure 14. After this, the speed dropped to the terminal 415 km s^{-1} speed that was derived from the best fit at larger heights.

7. Conclusions

The present analysis shows that CME observations that cover a large range of elongations (*e.g.*, from LASCO to SMEI or from SECCHI-COR to SECCHI-HI) require a more detailed treatment of the geometry of CME propagation than is the case for analysis of observations near the Sun (*e.g.*, LASCO). At large elongations, geometry significantly affects the determination of CME speed and trajectory. We examine the interaction of CME geometry with the properties of Thomson scattering and how this interaction affects CME brightness. Although not discussed here in detail, the impact on brightness will also affect CME mass determination. Finally, we present a detailed derivation of a method that accounts for geometry when deriving CME speed from elongation observations.

Fits of elongation versus time are compared to LASCO and SMEI observations as well as recent observations by SECCHI. Fits at constant speed provide good overlap with either LASCO or SMEI observations but cannot explain both data sets simultaneously. For the SECCHI example chosen, the constant speed fit is relatively good even in the HI-2 field of view and only a slight correction is required. This is mostly due to the slow CME speed at lower heights; a faster CME observed by SECCHI would provide a more robust test of these techniques.

Earlier work predicts that coronal drag will change a CME's speed as it moves through the heliosphere. We have used an *ad hoc* model $[\pm 0.5(d/2)^{3/4}\Delta V^2]$ to simulate the effect of coronal drag to produce speed profiles that yield improved fits to the elongation versus time profiles. Changes in CME speed may help explain the lack of a simple connection between some LASCO and SMEI events. Our continued analysis efforts will include LASCO, SMEI, and SECCHI observations at other time periods and the development of a more physically motivated coronal drag model.

Acknowledgements This work was sponsored by NASA Grant Nos. NNG05HL34I and NNG05GF98G and by LASCO and SECCHI MO&DA funding. SMEI is a collaborative project of the US Air Force Research Laboratory, NASA, the University of California at San Diego, the University of Birmingham (UK), Boston College, and Boston University. Financial support has been provided by the US Air Force, the University of Birmingham, and NASA. The STEREO/SECCHI project is an international consortium of the Naval Research Laboratory (USA), Lockheed Martin Solar and Astrophysics Lab (USA), NASA Goddard Space Flight Center (USA), Rutherford Appleton Laboratory (UK), University of Birmingham (UK), *Max-Planck-Institut für Sonnensystemforschung* (Germany), *Centre Spatial de Liège* (Belgium), *Institut d'Optique Théorique et Appliquée* (France), and *Institut d'Astrophysique Spatiale* (France). The Heliospheric Imager (HI) instrument was developed by a collaboration that included the Rutherford Appleton Laboratory and the University of Birmingham, both in the United Kingdom, the *Centre Spatial de Liège* (CSL), Belgium, and the US Naval Research Laboratory (NRL), Washington DC, USA. We also acknowledge use of the CME catalog that is generated and maintained at the CDAW Data Center by NASA and The Catholic University of America in cooperation with the Naval Research Laboratory (http://cdaw.gsfc.nasa.gov/CME_list). SOHO is a project of international cooperation between ESA and NASA.

References

Billings, D.E.: 1966, In: *A Guide to the Solar Corona*, Academic Press, New York.

Bisi, M.M., Jackson, B.V., Hick, P.P., Buffington, A., Odstrcil, D., Clover, J.M.: 2008, 3D reconstructions of the early-November 2004 CDAW geomagnetic storms: analyses of STELab IPS speed and SMEI density data. *J. Geophys. Res.* **113**, A00A11. doi:10.1029/2008JA013222.

Brueckner, G., Howard, R.A., Koomen, M.J., Korendyke, C.M., Michels, D.J., Moses, J.D., Soeker, D.G., Dere, K.P., Lamy, P.L., Llebaria, A., Bout, M.V., Sehwenn, R., Simnett, G.M., Bedford, D.K., Eyles, C.J.: 1995, The large angle and spectroseopie eoronagraph (LASCO). *Solar Phys.* **162**, 357–402.

Cargill, P.J.: 2004, On the aerodynamie drag foree acting on interplanetary coronal mass ejections. *Solar Phys.* **221**, 135–149.

Chen, J.: 1996, Theory of prominence eruption and propagation: interplanetary eonsequenees. *J. Geophys. Res.* **101**, 27499–27519.

Eyles, C.J., Siminett, G.M., Cooke, M.P., Jackson, B.V., Buffington, A., Hick, P.P., Waltham, N.R., King, J.M., Anderson, P.A., Holladay, P.E.: 2003, The Solar Mass Ejection Imager (SMEI). *Solar Phys.* **217**, 319–347.

Fisher, R.R., Lee, R.H., MaeQueen, R.M., Poland, A.I.: 1981, New Mauna Loa coronagraph systems. *Appl. Opt.* **20**, 1094–1101.

Gopalswamy, N., Lara, A., Yashiro, S., Kaiser, M., Howard, R.A.: 2001, Predieting the 1-AU arrival times of coronal mass ejeetions. *J. Geophys. Res.* **106**, 29207–29217.

Hayes, A.P., Vourlidas, A., Howard, R.A.: 2001, Deriving the eleetron density of the solar corona from the inversion of total brightness measurements. *Astrophys. J.* **548**, 1081–1086.

Howard, T.A., Simnett, G.M.: 2008, Interplanetary coronal mass ejections that are undeteeted by solar coronagraphs. *J. Geophys. Res.* **113**, A08102. doi:10.1029/2007JA012920.

Howard, T.A., Tappin, S.J.: 2008, Three-dimensional reconstruction of two solar eoronal mass ejections using the STEREO spaceeraft. *Solar Phys.* **252**, 373–383. doi:10.1007/s11207-008-9262-0.

Howard, T.A., Webb, D.F., Tappin, S.J., Mizuno, D.R., Johnston, J.C.: 2006, Tracking halo CMEs from 0–1 AU and space weather forecasting using the Solar Mass Ejection Imager (SMEI). *J. Geophys. Res.* **111**, A04105. doi:10.1029/2005JA011349.

Howard, T.A., Frey, C.D., Johnston, J.C., Webb, D.F.: 2007, On the evolution of coronal mass ejections om the interplanetary medium. *Astrophys. J.* **667**, 610–625.

Howard, R.A., Moses, J.D., Vourlidas, A., Newmark, J.S., Socker, D.G., Plunkett, S.P., *et al.*: 2008, Sun Earth Connection Coronal and Heliospheric Investigation (SECCHI). *Space Sci. Rev.* **136**, 67–115. doi:10.1007/s11214-008-9341-4.

Hundhausen, A.J., Burkepile, J.T., St. Cyr, O.C.: 1994, Speeds of coronal mass ejections: SMM observations from 1980 and 1984–1989. *J. Geophys. Res.* **99**, 6543–6552.

Jackson, B.V., Buffington, A., Hick, P.P., Altrock, R.C., Figueroa, S., Holladay, P.E., Johnston, J.C., Kahler, S.W., Mozer, J.B., Priee, S., Radick, R.R., Sagalyn, R., Sinelair, D., Simnett, G.M., Eyles, C.J., Cooke, M.P., Tappin, S.J., Kuchar, T., Mizuno, D., Webb, D.F., Anderson, P.A., Keil, S.L., Gold, R.E., Waltham, N.R.: 2004, The Solar Mass Ejection Imager (SMEI): The mission. *Solar Phys.* **225**, 177–207.

Kahler, S.W., Webb, D.F.: 2007, V-Arc coronal mass ejcctions observed with the Solar Mass Ejeetion Imager (SMEI). *J. Geophys. Res.* **112**, A09103. doi:10.1029/2007JA012358.

Koomen, M., Howard, R., Hansen, R., Hansen, S.: 1974, The coronal transient of 16 June 1972. *Solar Phys.* **34**, 447–452. *J. Geophys. Res.* **112**, A09103. doi:10.1029/2007JA012358.

Lugaz, N., Vourlidas, A., Roussev, I.I., Morgan, H.: 2009, Solar-terrestrial simulation in the STEREO Era: The 24–25 January 2007 eruptions. *Solar Phys.* **256**, 269–284.

Manchester, W.B., Vourlidas, A., Toth, G., Lugaz, N., Roussev, I.I., Sokolov, I.V., *et al.*: 2008, Three-dimensional MHD simulation of the 28 October 2003 coronal mas ejection: comparison with LASCO coronagraph observations. *Astrophys. J.* **684**, 1448–1460.

Manoharan, P.K.: 2006, Evolution of coronal mass ejection in the inner heliosphere: a study using white-light and scintillations images. *J. Geophys. Res.* **235**, 345–368.

Manoharan, P.K., Gopalswamy, N., Yashiro, S., Lara, A., Michalek, G., Howard, R.A.: 2004, Influence of coronal mass ejection interaetion on propagation of interplanetary shocks. *J. Geophys. Res.* **109**, A06109. doi:10.1029/2003JA010300.

McQueen, R.M.: 1974, The high altitude observatory white light eoronagraph experiment of Skylab. *J. Opt. Soc. Am.* **64**, 523–529.

Miehels, D.J., Howard, R.A., Koomen, M.J., Plunkett, S., Brueckner, G.E., Lamy, Ph., Schwenn, R., Bieseeker, D.A.: 1997. In: Wilson, A. (ed.) *Visibility of Earth-Directed Coronal Mass Ejections in Fifth SOHO Workshop: The Corona and Solar Wind Near Minimum Activity* **SP-404**, ESA, Oslo, 567–570.

Morrill, J.S., Howard, R., Webb, D.: 2006, Impacts of viewing geometry on CME observations in the heliosphere. *Bull. Am. Astron. Soc.* **38**, 231.

Morrill, J.S., Kunkel, V., Howard, R.A.: 2007, Kinematics of CMEs observed by LASCO and SECCHI. *Eos Trans. AGU* **88**(52), Fall Meet. Suppl., Abstract SH32A-0786.

Morrill, J., Kunkel, V., Halain, J., Harrison, R., Howard, R., Moses, J., Newmark, J., Plunkett, S., Socker, D., Wang, D., Vourlidas, A.: 2007, The impact of geometry on CME observations made by SEECHI. *Eos Trans. AGU* **88**(23), Jt. Assem. Suppl., Abstract SH41A-11.

Sheeley, N., Michels, D., Howard, R., Koomen, M.: 1980, Initial observations with the Solwind coronagraph. *Astrophys. J.* **237**, L99 – L101.

Sheeley, N., Herbst, A.D., Paltehi, C.A., Wang, Y.-M., Howard, R.A., Moese, J.D., *et al.*: 2008a, SECCHI observations of the Sun's garden-hose density spiral. *Astrophys. J.* **674**, L109 – L112.

Sheeley, N., Herbst, A.D., Paltehi, C.A., Wang, Y.-M., Howard, R.A., Moese, J.D., *et al.*: 2008b, Heliospheric images of the solar wind at earth. *Astrophys. J.* **675**, 853 – 862.

Tappin, S.J.: 2006, The deceleration of and interplanetary transient from the Sun to 5 AU. *Solar Phys.* **233**, 233 – 248.

Thernisien, A.F., Howard, R.A., Vourlidas, A.: 2006, Modeling of flux rope coronal mass ejections. *Astrophys. J.* **652**, 763 – 773.

van de Hulst, H.C.: 1950, *Bull. Astron. Inst. Neth.* **11**, 135 – 150.

Vourlidas, A., Howard, R.A.: 2006, The proper treatment of CME brightness: a new methodology and implication for observations. *Astrophys. J.* **642**, 1216 – 1221.

Wang, Y.-M., Sheeley, N.R.: 1994, Global evolution of interplanetary sector structure, coronal holes, and solar wind streams during 1976 – 1993: stackplot displays based on solar magnetic observations. *J. Geophys. Res.* **99**, 6597 – 6608.

Webb, D.F., Howard, R.A.: 1994, The solar cycle variation of coronal mass ejections and the solar wind. *J. Geophys. Res.* **99**, 4201 – 4220.

Webb, D.F., Mizuno, D.R., Buffington, A., Cooke, M.P., Eyles, C.J., Fry, C.D., *et al.*: 2006, Solar Mass Ejection Imager (SMEI) observation of coronal mass ejections (CMEs) in the heliosphere. *J. Geophys. Res.* **111**, A12101. doi:10.1029/2006JA011655.

Webb, D.F., Howard, T.A., Fry, C.D., Kuchar, T.A., Mizuno, D.R., Johnston, J.C., Jackson, B.V.: 2009, Studying geoeffective ICMEs between the sun and earth: space weather implications of SMEI observations. *Space Weather* **7**, S05002. doi:10.1029/2008SW000409.

Woo, R., Armstrong, J.W.: 1985, Doppler scintillations observations of interplanetary shocks within 0.3 AU. *J. Geophys. Res.* **90**, 154 – 162.